ACS APPLIED MATERIALS & INTERFACES

Research Article

Cite This: ACS Appl. Mater. Interfaces 2019, 11, 17979−17986

www.acsami.org

Low-Temperature Charging Dynamics of the Ionic Liquid and Its Gating Effect on $FeSe_{0.5}Te_{0.5}$ Superconducting Films

Cheng Zhang,[†,‡] Wei Zhao,[§] Sheng Bi,[§] Christopher M. Rouleau,[‡] Jason D. Fowlkes,[‡] Walker L. Boldman,[†] Genda Gu,[∥] Qiang Li,[∥] Guang Feng,[*,§,⊥] and Philip D. Rack[*,†,‡]

[†]Department of Materials Science and Engineering, University of Tennessee, Knoxville, Tennessee 37996, United States

[‡]Center for Nanophase Materials Sciences, Oak Ridge National Laboratory, Oak Ridge, Tennessee 37831, United States

[§]State Key Laboratory of Coal Combustion, School of Energy and Power Engineering, Huazhong University of Science and Technology (HUST), Wuhan 430074, China

[∥]Department of Condensed Matter Physics and Materials Science, Brookhaven National Laboratory, Upton, New York 11973, United States

[⊥]Shenzhen Research Institute of Huazhong University of Science and Technology, Shenzhen 518057, China

Supporting Information

ABSTRACT: Ionic liquids (ILs) have been investigated extensively because of their unique ability to form the electric double layer (EDL), which induces high electrical field. For certain materials, low-temperature IL charging is needed to limit the electrochemical etching. Here, we report our investigation of the low-temperature charging dynamics in two widely used ILs—DEME-TF_2N and C_4mim-TF_2N. Results show that the formation of the EDL at ∼220 K requires several hours relative to milliseconds at room temperature, and an equivalent voltage V_e is introduced as a measure of the EDL formation during the biasing process. The experimental observation is supported by molecular dynamics simulation, which shows that the dynamics are logically a function of gate voltage, time, and temperature. To demonstrate the importance of understanding the charging dynamics, a 140 nm thick $FeSe_{0.5}Te_{0.5}$ film was biased using the DEME IL, showing a tunable T_c between 18 and 35 K. Notably, this is the first observation of the tunability of the T_c in thick film $FeSe_{0.5}Te_{0.5}$ superconductors.

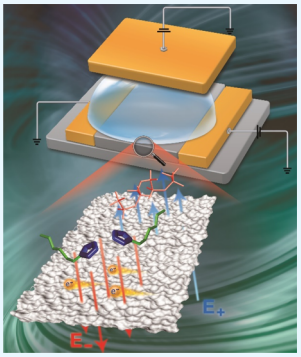

KEYWORDS: *ionic liquid, molecular dynamics simulation, 2D materials, iron-based superconductor*

INTRODUCTION

Ionic liquids (ILs) have been investigated extensively for their unique ability to form an electric double layer (EDL) at relatively low operating voltages.[1−4] When an external voltage is applied on the liquid, cations and anions are oriented to form an EDL at the IL−channel interface and support high electrical fields, which has been widely used to electrostatically gate carrier densities in field-effect transistors (FETs).[5−9] ILs have been used to extract and intercalate oxygen anions in oxide materials such as TiO_2, $SrTiO_3$, and MoO_3.[6,10−14] Recently, investigation of the electrostatic doping on superconducting materials has also been studied. Though the detailed underlying mechanism is not completely understood yet, it has been found in different superconductors that appropriate carrier doping can enhance the superconducting transition temperature (T_c).[4,15−23] *N*,*N*-Diethyl-*N*-methyl-*N*-(2-methoxyethyl)ammonium bis(trifluoromethanesulfonyl)-imide, known as DEME-TF_2N, is one of the commonly used ILs and demonstrated to work on both cuprate and iron-based superconductors to enhance T_c. However, it has also been noted that electrochemical etching can occur at certain voltage/temperature regimes for some IL-superconducting materials combinations.[20,22] One of the ways to avoid etching is to perform gate biasing at low temperature, typically 220 K, which is just slightly higher than the DEME IL glass-transition temperature (∼200 K). However, electrochemical etching can be minimized at low-temperature, ion migration rates, and thus, the EDL formation is also slower. Although many experiments have been demonstrated in the literature, very little is understood about the low-temperature charging dynamics—which is critical as the slow EDL formation can confuse the interpretation of low-temperature electrostatic doping studies.

In this report, we present our study of low-temperature charging dynamics of two ILs, DEME-TF_2N and C_4mim-TF_2N. C_4mim-TF_2N IL, also known as Bmim-TF_2N, has been commonly used in recent semiconductor gating studies. On the basis of these results, the gating effect on $FeSe_{0.5}Te_{0.5}$ (FST) thin films with the DEME IL is also investigated. FST belongs to the "11"-type iron-based superconductor, which has the simplest structure and lowest toxicity in the iron-based family. However, these iron chalcogenides have lower T_c

Received: February 7, 2019
Accepted: April 25, 2019
Published: April 25, 2019

DOI: 10.1021/acsami.9b02373
ACS Appl. Mater. Interfaces 2019, 11, 17979−17986

compared to iron arsenides. Thus, strategies have been made to enhance their T_c through different processing techniques, such as oxygen annealing and ion irradiation.[24−26] IL gating has also been studied on iron chalcogenides. Hanzawa et al. reported an investigation on FeSe thin films and showed that the onset superconducting transition temperature (T_c^{on}) can be enhanced from ∼8 to 35 K by applying V_g = 5.5 V to the DEME IL gate.[16] They found that the enhancement is realized on ∼10 nm thick FeSe films but not on those with 100 nm thickness. A similar study was done by Shiogai et al., where it was demonstrated that T_c of FeSe films can be enhanced by IL gating after electrochemical etching/thinning of the films.[20] FeSe in the form of exfoliated flakes has also been studied by Lei et al., where they used both IL gating and solid dielectric gating to enhance the T_c^{on} to an even higher temperature (∼45 K).[17,18] However, we are not aware of any studies showing IL T_c enhancement on the FST material in any form. FST has a zero resistance superconducting transition temperature (T_c^0) of ∼14 K for bulk crystals and >16 K in the thin-film form.[27−29] Our previous reports have shown that its T_c^0 can be further enhanced to ∼18 K by using a CeO_2 buffer layer.[30,31] Thus, we investigated whether IL gating can enhance the superconducting properties of FST thin films, which intrinsically have a higher T_c than FeSe.

RESULTS AND DISCUSSION

Ions inside the pristine IL before bias are randomly distributed. Once a positive V_g is applied, cations and anions migrate to form an EDL on the anode and cathode, respectively. Similar to charging a capacitor, during this IL charging process, a current flow, I_g, is detected because of the migration of the ions. Once the EDL saturates, I_g becomes zero. If V_g is released to zero, then the oriented ions will tend to move back to an equilibrium state because of their mutual Coulomb repulsion. This charging and releasing process happens on the milliseconds time scale at room temperature; however, at a low temperature, longer time is needed because of the low ion migration rates at higher viscosity. To understand the EDL dynamics at low temperature, we introduce an equivalent voltage V_e. It is defined as the value of applied external V_g, in which I_g drops below 0.1 nA or slightly switches polarity and thus represents a pseudo-saturated state of the EDL. For example, when biased at V_g = 5 V as a function of time, V_e will start at 0 V and increases toward 5 V as the ions migrate to each electrode. Importantly, the dynamics of V_e as a function of time is strongly temperature-dependent. To measure the V_e at a certain time during the biasing process, we lower the externally applied V_g until the pseudo-saturated state is reached. Under this scheme, when $V_g > V_e$, charging occurs and a positive current flow will be detected and vice versa. Figure 1 schematically illustrates the EDL charging (left panel) and decharging (right panel) when $V_g > V_e$ and $V_g < V_e$, respectively.

To understand the low-temperature charging dynamics of DEME IL, the time-dependent I_g and V_e were measured for different-sized IL droplets. A typical IL test setup is shown in Figure 2a, and a detailed description can be found in Methods section. Figure 2b shows the plot of normalized current density as a function of time under 5 V constant gate biasing, measured at 220 and 210 K. As expected, higher temperature results in larger average current flow, and both experience an exponential decay, as shown in fitted dashed lines in Figure 2b, in the accumulation of the EDL ion density. To confirm this, we also

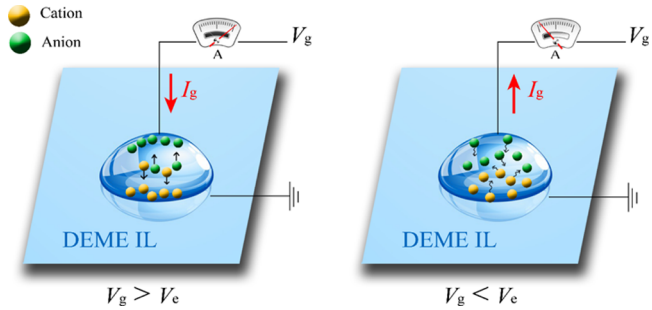

Figure 1. Schematic of low-temperature EDL dynamics of DEME-TF_2N IL under positive gate bias. When $V_g > V_e$, current flows during the formation of the EDL (left panel); to measure the V_e of the EDL, the gate voltage is incrementally lowered until the applied V_g drops below V_e. At this point, the current drops below 0.1 nA (and changes polarity), which is interpreted as ion migration from the EDL and a decrease in the ion concentration in the EDL (right panel).

measured V_e, as described above, as a function of time. Figure 2c illustrates the time dependence of V_e (left axis) compared to the integrated charge density (right axis, log scale), which both show the dynamics of the EDL formation. The accumulated charge density was calculated from Figure 2b by integrating I_g over time, based on the assumption that all charge is accumulated in the EDL. Interestingly, the charging rate increases logarithmically, whereas the effective voltage increases on a more linear scale. We attribute this to the fact that multiple ion layers are being formed and ions accumulating further from the IL/anode interface contribute less to the effective voltage/field in the material.

Another test with 3 V biasing at two temperatures was conducted, and the result is shown in Figure 3a,b. As expected, the V_e increases slowly at a lower voltage; however, after 180 min at 220 K, V_e only reaches 2.55 V, which is a higher fraction of the applied voltage (85%) relative to the 5 V applied bias where $V_e \approx 2.8$ V (56%) in the same time and same temperature. The integrated charge densities are also plotted on the second *y*-axis in Figure 3b, which have a similar logarithmic functionality as the 5 V data in Figure 2c, but, as-expected, with a smaller magnitude for each temperature. Another measurement was performed at a higher temperature of 245 K biased with 3 V gate voltage, and the result is shown in Figure 3c. At this temperature, the magnitude of I_g is much higher, and it decays differently where a "bump" is observed. This behavior is likely due to the electrochemical etching, which has been reported by Shiogai et al.[20] Interestingly, V_e does not appear to increase compared to that biased at 220 K. Either the viscosity change is not significant over this 25 K change or part of energy is consumed on etching instead of the EDL formation. Discoloration of the copper tape was observed in the 245 K measurement, which is noted in the optical micrograph (Figure 3c inset) where the IL is cleaned off the tape. We note that the calculated integrated charge density shown in Figure 3b is very high, ranges from $\sim 10^{-4}$ to $\sim 10^{-2}$ C/cm^2 during the 3 h biasing at 220 K, which corresponds to 10^{15} to 10^{17} cm^{-2} charge carriers, respectively. This is at least 2 orders of magnitude higher than the surface charge carrier densities reported.[1,8,23,32] The higher integrated charges could be attributed to multiple ion layers formed near the interface region,[33,34] though V_e is mostly affected by the ion layers that are close to the IL−solid interface. Similar tests were performed using another popular IL, C_4mim-TF_2N, and the

DOI: 10.1021/acsami.9b02373
ACS Appl. Mater. Interfaces 2019, 11, 17979−17986

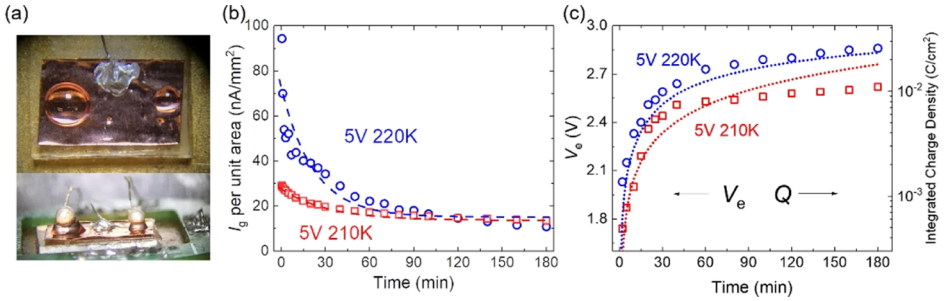

Figure 2. Time-dependent gate current (I_g) and equivalent voltage (V_e) in DEME IL with an applied gate voltage of 5 V, measured at 210 and 220 K. A typical sample setup for the measurement is shown in (a). Droplets with varied sizes were tested, and the current density, normalized based on the droplet projected area, as a function of time is plotted in (b); dashed lines are exponential decay fittings $I_g = A\exp(x/t) + B$. The measured V_e as a function of time is shown in (c) (red squares and blue circles, left axis); note that the integrated charge density increases logarithmically (dotted lines, right axis) andV_e increases much slower.

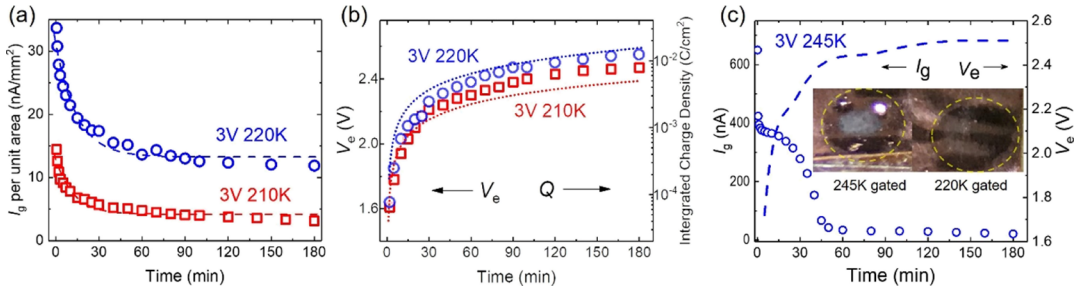

Figure 3. I_g and V_e in DEME IL monitored over time with different applied gate voltage and temperature. With a lower V_g of 3 V, the time-dependent I_g and V_e (open circles and squares) are plotted in (a,b), respectively; note at 220 K with a lower I_g, V_e increases slowly and yields at around 2.5 V after 3 h. Dashed lines in (a) are the exponential fittings of I_g, and dotted lines in (b) show the integration of I_g over time. (c) shows the result of the measurement with V_g = 3 V at 245 K, with I_g in circles, and V_e as dashed line; note the high current and an abnormal discontinuity in the I_g decay, which is likely due to electrochemical etching. The inset in (c) is compared with the optical images of 245 K biased area and 220 K biased area, where a noticeable etching effect at 245 K on the copper tape is clearly seen. Yellow dashed circle indicates the area covered by IL droplets. The result of similar tests on another IL C_4mim-TF_2N can be found in the Supporting Information.

result can be found in the Supporting Information (Figures S1 and S2). The charging dynamics of different IL drop sizes was also conducted, and the results are shown in Figure S3.

To qualitatively investigate the charging dynamics, MD simulations were performed on the system consisting of $[C_4mim][Tf_2N]$ IL and Ag/Cu electrodes with implementation of constant potential method (CPM)[35] to mimic the applied gate voltage. Figure 4a schematically illustrates the

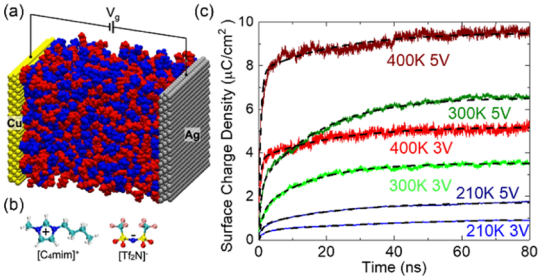

Figure 4. (a) Schematic illustrating the molecular dynamics (MD) simulation setup. The yellow and gray spheres, respectively, represent the Cu and Ag electrodes, and red and blue spheres between Cu and Ag electrodes denote the cation and anion in $[C_4mim][Tf_2N]$ IL, respectively. (b) Atomic configuration of the $[C_4mim]^+$ cation and $[Tf_2N]^-$ anion. (c) Time evolution of surface charge density under different temperatures (210, 300, and 400 K) and different gate voltages of 3 and 5 V. Note that in (c), the surface charge density is negative but shown as its absolute value for clarity. The dashed lines represent the fitting curves of MD data of the charging process.

system of MD simulation, and Figure 4b shows the atomic configuration of the cation and anion. Analyzed from MD simulation, the surface charge density of the EDL at the (−) copper electrode is exhibited in Figure 4c as a function of time simulated at two potentials (3 and 5 V) and three temperatures (210, 300, and 400 K). The cumulative charge density is solved via the Poisson equation by accounting for all the anion/cation layers relative to the metal surface. The dynamics of the EDL formation could be characterized by the response of surface charge density, $Q(t)$, on the electrode surface and fitted by the exponential functions[36]

$$Q(t) = Q_{max}[1 - a\exp^{-t/b} - (1 - a)\exp^{-t/c}] \quad (1)$$

where Q_{max} is the electrode surface charge density of the EDL in a pseudo-equilibrium and a, b are fitting parameters for the fast exponential and $(1 - a)$ and c are fitting parameters for the slow surface charging exponential (see Table S1 for a summary of the fitting parameters). Note for the 210 K data that the dynamics are much slower and equilibrium is not reached, particularly for the 3 V data, during the 80 ns simulation time; however, the data fit reasonably well with eq 1. The initial clear trends displayed in Figure 4c are as follows: (1) Q_{max} increases with increasing temperature, (2) for each temperature, higher voltage increases Q_{max}, and (3) the increasing temperature and voltage increases the charging rate; all of these observations are consistent with experimental observations. In particular, for the effects of temperature on EDL capacity (i.e., the charge accumulated on the surface), there are studies reporting

DOI: 10.1021/acsami.9b02373
ACS Appl. Mater. Interfaces 2019, 11, 17979−17986

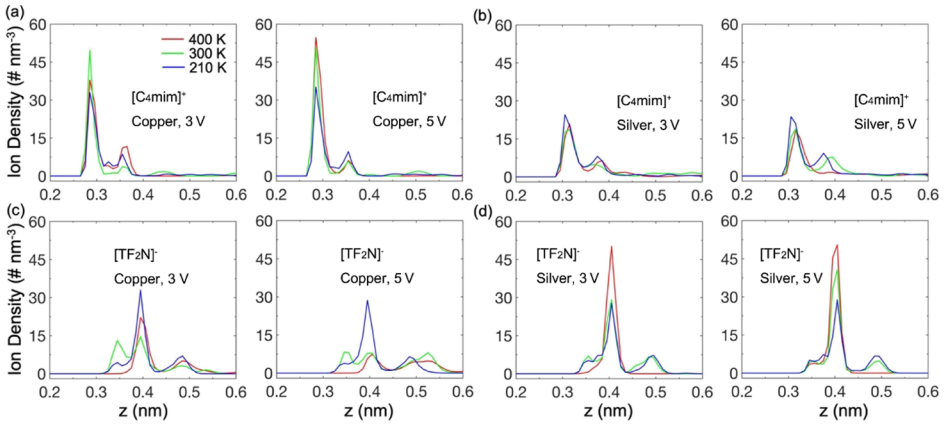

Figure 5. Number density as a function of distance for $t = t_{max}$ for ions near the copper electrode (a,c) and silver electrode (b,d). (a,b) are for the $[C_4mim]^+$ cation and (c,d) for the $[Tf_2N]-$ anion. Left columns in (a−d) are distributions under a 3 V gate bias, and right columns refer to a 5 V gate bias. z = 0 nm denotes the position of copper and silver surfaces which are close to ILs.

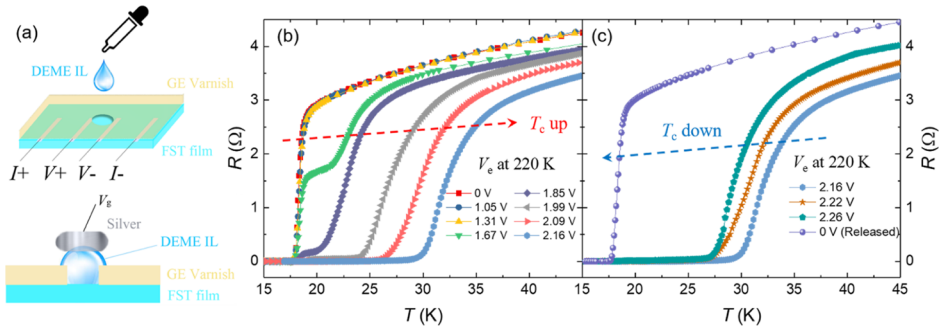

Figure 6. Temperature-dependent resistance of the FST film as a function of DEME IL equivalent voltages. Schematic illustrating the four-point probe FST device used in R vs T measurements is shown in (a). The FST film with the DEME IL reservoir between the voltage leads is cooled down to 220 K before the gate bias (3 V) was applied. The superconducting transition as a function of increasing V_e is shown in (b,c). T_c^0 and T_c^{on} of the pristine film are 17.8 and 18.7 K, which increase up to 30 and 35 K, respectively, as the V_e increases to 2.16 V. Higher V_e suppresses T_c, which is likely due to overdoping. After setting V_g = 0 bias overnight, V_e drops to zero and T_c is recovered back to its pristine value.

possible temperature dependences: the temperature could decrease,[37,38] increase,[39,40] or slightly change the capacity.[41,42] Herein, the increase of Q_{max} with increasing temperature may originate from the weakened ion association in EDL, which has also been observed in previous studies.[39,40,43] While the 210 K charge density is universally smallest and 5 V > 3 V at all times, the 400 K—3 V condition initially charges faster than the 300 K—5 V condition ($b_{400K,3V}$ = 0.412 ns < $b_{300K,5V}$ = 0.7586 ns) at longer times (>10 ns) and the 300 K—5 V condition has a higher surface charge density and ultimately a higher Q_{max}. Thus, the simulations confirm what the experimental data revealed, namely, the surface charge density is a function of the applied voltage, temperature, and charging time.

Figure 5 illustrates the number density as a function of position for the three temperatures for the $[C_4mim]^+$ cation (Figure 5a,b) and the $[Tf_2N]^-$ anion (Figure 5c,d) near the negatively charged copper electrode (Figure 5a,c) and the positively charged silver electrode (Figure 5b,d) at $t = t_{max}$ for 3 and 5 V, respectively. At 3 V, the $[C_4mim]^+$ cations appear to have three dominant orientations with peaks at 0.29, 0.36, and 0.44 nm, while the first layer of $[Tf_2N]^-$ anions have peaks at 0.35, 0.40, and 0.49 nm. The orientations of ion peaks could be seen in Figure S4, which show that both the cation and anion in the first peak prefer to be parallel to the electrode surface, and on moving further from the electrode surface, the ion would be tilted. As seen in Figure 5, at 3 V, the 0.29 nm peak is slightly higher at 300 K than at 400 K, and the 0.36 nm peak is higher at 400 K than at the 300 K orientation. Therefore, on the basis of the cation contribution, one expects the surface charge of the 300 K orientation to be higher. However, when the $[Tf_2N]^-$ anion distributions are compared, the 0.35 nm peak is also found to be much higher at 300 K than at 400 K, which counterbalances the cation charge density and results in 400 K having a higher overall surface charge density. Similar arguments can be made for the 210 K—3 V condition; namely, the overall $[C_4mim]^+$ cation density is slightly lower and has a higher total $[Tf_2N]^-$ anion density for the dominant orientations relative to 400 K. At 5 V, the $[C_4mim]^+$ cation distributions at 0.29 nm increase for all temperatures and the overall $[Tf_2N]^-$ anion distribution shifts to longer distance relative to 3 V; both of which lead to higher overall surface charge density. While the specific ion distributions and surface charge densities are realized at the much longer and larger experimental conditions, the simulations illustrate that the total surface charge density is determined by both the resultant anion and cation distributions; experimentally, these distributions are a function of the applied voltage, temperature, and charging time.

On the basis of the above investigation, we studied the IL-biasing effect on FST films to establish the relationship between V_e and T_c. The film samples were prepared as described in the Methods section and illustrated in Figure 6a. RT measurements as a function of V_e values are plotted in Figure 6b,c. At zero bias, the FST film has a T_c^0 = 17.8 K and

DOI: 10.1021/acsami.9b02373
ACS Appl. Mater. Interfaces 2019, 11, 17979−17986

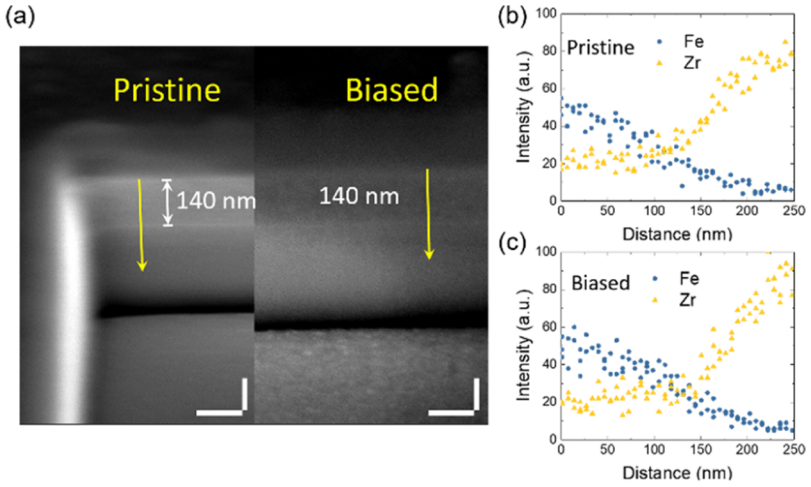

Figure 7. Tilted scanning electron microscopy image of pristine and the biased area of an FST film and EDS line scan along the thickness direction. A biased FST film was FIB-milled and imaged in a scanning electron microscope on a 45° tilted stage. The images are compared to a pristine and biased area of the film in (a), with no observable thickness change for the IL-biased region. (b,c) are EDS line scans of Fe (film) and Zr (substrate) in pristine and biased areas, respectively, along the thickness direction [yellow arrow in (a)]. White scale bars in (a) show 100 nm length in horizontal and vertical directions.

T_c^{on} = 18.7 K, which is consistent with our previous reports.[31] Various V_e values were obtained by charging the IL at 3 V gate bias over time (see Methods section for details); importantly during the *RT* measurements when T < 220, V_e remains essentially constant because below the glass-transition temperature, the EDL charging process is significantly slowed as the viscosity increases. As demonstrated in Figure 6b, the RT curves are not affected when V_e < 1.67 V. When V_e reaches 1.67 V, an enhancement of T_c is observed, as evidenced by the two-step superconducting transition. This indicates that only part of the channel layer is electrostatically doped and the superconducting phase starts to form at higher temperature; T_c^0, however, does not change, indicating that the superconducting phase is not continuous over the entire channel region. This two-step transition was also observed in previous IL-biasing studies on FeSe.[16,17,20] As V_e is increased, the T_c^{on} is shifted to higher temperature and the T_c^0 remains unchanged until V_e = 2.09 V (see Figure S5 a for the magnified view of the low-resistance region), where the two-step transition disappears and a single transition is realized. At V_e = 2.16 V, the T_c^0 and T_c^{on} reach the highest value of 30 and 35 K, respectively. Further increase in V_e suppresses the T_c, which may indicate that the film is overdoped. To test the reversibility superconducting properties, the applied gate bias was set to zero at 220 K after the test and the effective voltage was allowed to decay overnight. The T_c^0 and T_c^{on} are recovered back to 18 and 19 K, respectively, with a normal state resistance value similar to the initial measurement.

T_c enhancements of FeSe thin films and exfoliated single-crystal flakes have been previously explored via DEME IL biasing. All previously reported enhancements were done on ultrathin films/flakes with the thickness around or lower than 10 nm. Shiogai et al. reported that the T_c of FeSe films cannot be enhanced by biasing until being etched down to a few nanometer thickness.[20] To confirm that our films were not electrochemically etched during the gate biasing, the biased film was focused ion beam (FIB)-milled at multiple sites in the pristine and IL-biased region and subsequently imaged as shown in Figure 7a. The thickness of the biased film is ∼140 nm, which is the same as the pristine film—no observable etching occurred during biasing. To confirm the layer identification, Energy Dispersive X-ray Spectroscopy (EDS) line scans were performed along the thickness direction, and the result of pristine and the biased area is shown in Figure 7b,c, respectively. Fe and Zr were selected to indicate the FST film and the yttrium-stabilized zirconia oxide (YSZ) substrate, respectively.

Figure 7 confirms that the IL-biasing process at 220 K does not etch the FST film. Compared to FeSe for which T_c IL-biasing enhancements were only observed in ultrathin films/flakes, our study shows that this IL-gating T_c enhancements are applicable to >100 nm thickness. Although this could be due to intrinsic differences in FeSe versus FST, it could also be related to the EDL dynamics discussed above. Things are also complicated for ultrathin FeSe films approaching a few layers as interface or strain effects could also contribute to increasing higher T_c.[44,45] Interestingly, while FST thin films have a higher intrinsic T_c than FeSe, the enhanced T_c due to IL biasing reaches the similar value of 35−40 K. It is reasonable to speculate that chemical doping and IL gating are complementary and that Te doping in FST contributes a partial chemical doping as well as the IL gating further electrostatically dopes the lattice. Note that the highest tunable T_c of FeSe gating is reported at ∼48 K with a Li solid gate biasing,[18] where the enhancing effect is attributed to not only electrostatic doping but also the Li intercalation, which has been reported on other FET IL studies.[6] The highest T_c in FST is achieved at V_e = 2.16 V, and we surmise that FeSe would need a higher V_e to electrostatically maximize its T_c value to 35 K. According to the low-temperature EDL charging dynamics discussed above, V_e the effective IL bias is a strong function of temperature, applied voltage, and time. Thus, to elucidate the effects of electrostatic doping via IL gating at low temperature, significant care must be taken to clearly understand EDL dynamics.

CONCLUSIONS

Low-temperature dynamics of the IL EDL has been investigated. The state of the EDL is logically a function of gate voltage, time, and temperature. At 210 and 220 K, long

DOI: 10.1021/acsami.9b02373
ACS Appl. Mater. Interfaces 2019, 11, 17979−17986

times are required for the EDL to form in the IL. The concept of equivalent voltage V_e is introduced as a measure of the EDL formation during the low-temperature biasing process. MD simulations were conducted, and the results are qualitatively consistent with the experimental observation. To demonstrate the importance of understanding the charging dynamics, a 140 nm thick FST film was biased using the DEME IL and its onset T_c can be tuned from 18 to a maximum of 35 K for $0 \leq V_e \leq 2.16$ V and is apparently overdoped when $V_e > 2.16$ V.

METHODS

IL Test. DEME-TF_2N IL was purchased from Sigma-Aldrich. Low-temperature dynamic tests were conducted using copper tape as the substrate. A ground wire was connected on the copper using silver paint. IL droplets with various sizes were put on the copper tape and gate electrodes were made with silver epoxy, which was subsequently suspended on the liquid (Figure 2a). The sample was put into a Quantum Design Physics Property Measurement System (PPMS) to conduct electrical measurements. Two Keithley 2400 sources were used to apply gate voltages V_g = 3 and 5 V at 210 and 220 K, while the gate current I_g was monitored for up to 3 h. During the low-temperature biasing, an equivalent gate voltage V_e was periodically determined by lowering the applied V_g in 0.01 V steps until I_g < 0.1 nA (and typically switched polarity to negative current).

Measurement of Effective Voltage V_e. As the V_e measurements are important to understand, here we overview the specific experimental procedure. Each V_e measurement takes less than 15 s, and during each measurement, we stop timing the charging time until the V_g is restored. In detail, at the beginning of each measurement, V_g is lowered in ~0.1 V increments per half second, while the current flow is monitored. When the gate drops below 1 nA, V_g is lowered at a smaller increment of 0.01 V at ~1 s time intervals until the gate current approaches the instrumentation limit of ~10 pA and eventually I_g turns to negative. The V_g at the negative current crossover point is recorded as the effective voltage V_e. Then the V_g is directly set back to 3 or 5 V, and we continue to record the charging time. The actual "discharging" time is very brief, and the driving force is very small as the voltage drop below V_e is <0.01 V. The integrated charge during this negative I_g is negligible relative to the total charging process. Thus, if taking −100 pA current to integrate over the cumulative time of the negative charge (~2 s), the EDL charge dissipation is only $\sim 5 \times 10^{-9}$ C/cm^2 for each V_e measurement, relative to the cumulative EDL charging at the level of 10^{-2} C/cm^2.

MD Simulation. Figure 4a shows the MD system which consists a slab of room-temperature IL [C_4mim][Tf_2N] enclosed between Ag(111) and Cu(111) electrodes. The electrodes have an area of 6.0 × 6.0 nm^2 in the *xy*-plane and were separated by 8.0 nm in *z*-direction, which is wide enough to produce a bulklike IL region in the middle of the system. The gate voltage applied between electrodes was maintained using the CPM during the simulation[35] because CPM could correctly mimic the charging process[36] and also take into account the electronic polarizability of pore walls, in agreement with other models of polarizable electrodes.[46,47] The electrode potential was applied on a plane across the center of surface atoms, and the number of ion pairs inside the channel was tuned to ensure the ILs in central part of the channel maintaining a bulklike state. An all-atom model was adopted for the IL [C_4mim][Tf_2N],[48] and the force fields for the electrodes were taken from ref 49, which can render accurate interfacial properties at the face-centered cubic metal surface. Through the implementation of CPM, MD simulations were performed via a customized GROMACS code in the canonical ensemble,[50] with a time step of 2 fs. The chemical bonds including the H-atom in RTILs were constrained by the linear constraint solver (LINCS) algorithm.[51] Three different temperatures of ILs (400, 300, and 210 K) were coupled with the velocity rescaling thermostat.[52] The electrostatic interactions were computed using the particle mesh Ewald method[53] with a fast Fourier transform grid spacing of 0.1 nm and cubic interpolation for charge distribution. The cutoffs for both Coulombic and van der Waals interactions are 1.2 nm. Each simulation was first run for 10 ns to reach equilibrium, and then an 80 ns production run was performed for analysis. It is worthy to note that the glass-transition temperature (T_g) of [C_4mim][Tf_2N] is about 187 K,[54−56] and the phase transitions in confined ILs occur at a lower temperature compared to bulk ILs.[57−59] Therefore, the lowest temperature (210 K) used in MD simulations in this work would keep the IL away from the glass transition, especially when it is confined at the solid surface. However, the low temperature of 210 K would significantly reduce the ion diffusion, which would make the charging process much slower during the limited simulation time, while at high temperatures of 300 and 400 K, the surface charge could reach an equilibrium state within 80 ns. To ensure the accuracy of the charging process data, each case was repeated 10 times with different initial configurations for analysis.

FST Superconducting Film Test. FST thin films were epitaxially grown on a single-crystalline YSZ substrate, with a CeO_2 buffer layer. The detailed growth conditions can be found in our previous reports.[25,31,60] In-line-four-point contacts were made on the film surface using silver paint and gold wires. The film was then covered by GE varnish, leaving a 0.4 mm by a 0.5 mm hole between two voltage leads to act as a reservoir/well for contact with the IL (Figure 6a). The four-point probe FST film was then measured in the PPMS after various V_g holding times to establish various V_e. Multiple steps of electrostatic biasing were performed at 220 K with V_g = 3 V. After each gate biasing step, the sample was cooled down to 5 K and the resistance versus temperature (*RT*) curve was measured by warming up to 220 K. V_e for each measured curve was measured, as described above, after the temperature reached 220 K. Notably, V_e is stable during the temperature drop and *RT* curve measurement as the IL drops below glass-transition temperature. T_c^0 is determined by the temperature at which the resistance reached 1% of its normal state resistance. T_c^{on} is determined by the intersection of the extrapolated normal state *RT* curve and the linearly fitted superconducting transition region of the *RT* curve (Figure S5). FIB milling and subsequent imaging were conducted using an FEI 600 Nova dual scanning electron/ion microscope to mill the pristine and biased film to monitor any electrochemical etching during IL biasing. High-resolution cross-sectional secondary electron images and EDS line scans were taken using a Zeiss Merlin scanning electron microscope.

ASSOCIATED CONTENT

Supporting Information

The Supporting Information is available free of charge on the ACS Publications website at DOI: 10.1021/acsami.9b02373.

Charging dynamic tests for DEME IL, additional MD results, and details of FST IL test (PDF)

AUTHOR INFORMATION

Corresponding Authors

*E-mail: gfeng@hust.edu.cn (G.F.).
*E-mail: prack@utk.edu (P.D.R.).

ORCID

Cheng Zhang: 0000-0001-6531-4703
Wei Zhao: 0000-0003-1497-9312
Sheng Bi: 0000-0001-8804-7353
Guang Feng: 0000-0001-6659-9181
Philip D. Rack: 0000-0002-9964-3254

Author Contributions

C.Z. and P.D.R. designed this study. W.Z., S.B., and G.F. conducted MD simulation and analysis. G.G. grew the FST target crystal. C.Z. and Q.L. made the FST film. C.Z., W.L.B., and C.M.R. did the sample preparation and the PPMS measurements. J.D.F. and C.Z. carried out FIB and EDS studies. C.Z., P.D.R, and G.F. wrote the manuscript. All

DOI: 10.1021/acsami.9b02373
ACS Appl. Mater. Interfaces 2019, 11, 17979−17986

authors contributed to discuss and comment on the manuscript.

Notes

The authors declare no competing financial interest.

■ ACKNOWLEDGMENTS

C.Z. and P.D.R. acknowledge support by U.S. Department of Energy (DOE) under grant DE-SC0002136. W.Z., S.B., and G.F. thank support from the National Natural Science Foundation of China (51876072). C.M.R. and J.D.F. acknowledge support by the Center for Nanophase Materials Sciences, which is a DOE Office of Science User Facility. W.B. acknowledges support from NSF (grant #1544686). FST superconducting films were made at Brookhaven National Laboratory. Q.L. and G.G. were supported by the Office of Basic Energy Sciences, Division of Materials Sciences and Engineering, US Department of Energy under contract no. DE-SC0012704. The authors also acknowledge that the device fabrication and electrical measurements were conducted at the Center for Nanophase Materials Sciences, which is a DOE Office of Science User Facility. G.F. also acknowledges support from Shenzhen Basic Research Project (JCYJ20170307171511292). All MD simulations were performed at the National Supercomputing Centers in Guangzhou (Tianhe II).

■ REFERENCES

(1) Nakano, M.; Shibuya, K.; Okuyama, D.; Hatano, T.; Ono, S.; Kawasaki, M.; Iwasa, Y.; Tokura, Y. Collective Bulk Carrier Delocalization Driven by Electrostatic Surface Charge Accumulation. *Nature* **2012**, *487*, 459−462.

(2) Ueno, K.; Nakamura, S.; Shimotani, H.; Ohtomo, A.; Kimura, N.; Nojima, T.; Aoki, H.; Iwasa, Y.; Kawasaki, M. Electric-Field-Induced Superconductivity in an Insulator. *Nat. Mater.* **2008**, *7*, 855−858.

(3) Jeong, J.; Aetukuri, N.; Graf, T.; Schladt, T. D.; Samant, M. G.; Parkin, S. S. P. Suppression of Metal-Insulator Transition in VO_2 by Electric Field−Induced Oxygen Vacancy Formation. *Science* **2013**, *339*, 1402−1405.

(4) Ueno, K.; Nakamura, S.; Shimotani, H.; Yuan, H. T.; Kimura, N.; Nojima, T.; Aoki, H.; Iwasa, Y.; Kawasaki, M. Discovery of Superconductivity in $KTaO_3$ by Electrostatic Carrier Doping. *Nat. Nanotechnol.* **2011**, *6*, 408−412.

(5) Kötz, R.; Carlen, M. Principles and Applications of Electrochemical Capacitors. *Electrochim. Acta* **2000**, *45*, 2483−2498.

(6) Zhang, C.; Pudasaini, P. R.; Oyedele, A. D.; Ievlev, A. V.; Xu, L.; Haglund, A. V.; Noh, J. H.; Wong, A. T.; Xiao, K.; Ward, T. Z.; Mandrus, D. G.; Xu, H.; Ovchinnikova, O. S.; Rack, P. D. Ion Migration Studies in Exfoliated 2D Molybdenum Oxide via Ionic Liquid Gating for Neuromorphic Device Applications. *ACS Appl. Mater. Interfaces* **2018**, *10*, 22623−22631.

(7) Ye, J. T.; Inoue, S.; Kobayashi, K.; Kasahara, Y.; Yuan, H. T.; Shimotani, H.; Iwasa, Y. Liquid-gated Interface Superconductivity on an Atomically Flat Film. *Nat. Mater.* **2010**, *9*, 125−128.

(8) Yamada, Y.; Ueno, K.; Fukumura, T.; Yuan, H. T.; Shimotani, H.; Iwasa, Y.; Gu, L.; Tsukimoto, S.; Ikuhara, Y.; Kawasaki, M. Electrically Induced Ferromagnetism at Room Temperature in Cobalt-Doped Titanium Dioxide. *Science* **2011**, *332*, 1065−1067.

(9) Uesugi, E.; Goto, H.; Eguchi, R.; Fujiwara, A.; Kubozono, Y. Electric Double-Layer Capacitance Between an Ionic Liquid and Few-Layer Graphene. *Sci. Rep.* **2013**, *3*, 1595.

(10) Black, J. M.; Come, J.; Bi, S.; Zhu, M.; Zhao, W.; Wong, A. T.; Noh, J. H.; Pudasaini, P. R.; Zhang, P.; Okatan, M. B.; Dai, S.; Kalinin, S. V.; Rack, P. D.; Ward, T. Z.; Feng, G.; Balke, N. Role of Electrical Double Layer Structure in Ionic Liquid Gated Devices. *ACS Appl. Mater. Interfaces* **2017**, *9*, 40949−40958.

(11) Leng, X.; Pereiro, J.; Strle, J.; Dubuis, G.; Bollinger, A. T.; Gozar, A.; Wu, J.; Litombe, N.; Panagopoulos, C.; Pavuna, D.; Božović, I. Insulator to Metal Transition in WO_3 Induced by Electrolyte Gating. *npj Quantum Mater.* **2017**, *2*, 35.

(12) Li, M.; Han, W.; Jiang, X.; Jeong, J.; Samant, M. G.; Parkin, S. S. P. Suppression of Ionic Liquid Gate-Induced Metallization of $SrTiO_3$(001) by Oxygen. *Nano Lett.* **2013**, *13*, 4675−4678.

(13) Jeong, J.; Aetukuri, N. B.; Passarello, D.; Conradson, S. D.; Samant, M. G.; Parkin, S. S. P. Giant Reversible, Facet-Dependent, Structural Changes in a Correlated-Electron Insulator Induced by Ionic Liquid Gating. *Proc. Natl. Acad. Sci. U.S.A.* **2015**, *112*, 1013−1018.

(14) Altendorf, S. G.; Jeong, J.; Passarello, D.; Aetukuri, N. B.; Samant, M. G.; Parkin, S. S. P. Facet-Independent Electric-Field-Induced Volume Metallization of Tungsten Trioxide Films. *Adv. Mater.* **2016**, *28*, 5284−5292.

(15) Ye, J. T.; Zhang, Y. J.; Akashi, R.; Bahramy, M. S.; Arita, R.; Iwasa, Y. Superconducting Dome in a Gate-Tuned Band Insulator. *Science* **2012**, *338*, 1193−1196.

(16) Hanzawa, K.; Sato, H.; Hiramatsu, H.; Kamiya, T.; Hosono, H. Electric Field-Induced Superconducting Transition of Insulating FeSe Thin Film at 35 K. *Proc. Natl. Acad. Sci. U.S.A.* **2016**, *113*, 3986−3990.

(17) Lei, B.; Cui, J.; Xiang, Z.; Shang, C.; Wang, N.; Ye, G.; Luo, X.; Wu, T.; Sun, Z.; Chen, X. Evolution of High-Temperature Superconductivity From a Low-T_c Phase Tuned by Carrier Concentration in FeSe Thin Flakes. *Phys. Rev. Lett.* **2016**, *116*, 077002.

(18) Lei, B.; Wang, N. Z.; Shang, C.; Meng, F. B.; Ma, L. K.; Luo, X. G.; Wu, T.; Sun, Z.; Wang, Y.; Jiang, Z.; Mao, B. H.; Liu, Z.; Yu, Y. J.; Zhang, Y. B.; Chen, X. H. Tuning Phase Transitions in FeSe Thin Flakes by Field-Effect Transistor with Solid Ion Conductor as the Gate Dielectric. *Phys. Rev. B* **2017**, *95*, 020503.

(19) Lei, B.; Xiang, Z.; Lu, X.; Wang, N.; Chang, J.; Shang, C.; Zhang, A.; Zhang, Q.; Luo, X.; Wu, T. Gate-Tuned Superconductor-Insulator Transition in (Li, Fe) OHFeSe. *Phys. Rev. B* **2016**, *93*, 060501.

(20) Shiogai, J.; Ito, Y.; Mitsuhashi, T.; Nojima, T.; Tsukazaki, A. Electric-Field-Induced Superconductivity in Electrochemically Etched Ultrathin FeSe Films on $SrTiO_3$ and MgO. *Nat. Phys.* **2016**, *12*, 42−46.

(21) Bollinger, A. T.; Dubuis, G.; Yoon, J.; Pavuna, D.; Misewich, J.; Božović, I. Superconductor−Insulator Transition in $La_{2-x}Sr_xCuO_4$ at the Pair Quantum Resistance. *Nature* **2011**, *472*, 458.

(22) Ueno, K.; Shimotani, H.; Yuan, H.; Ye, J.; Kawasaki, M.; Iwasa, Y. Field-Induced Superconductivity in Electric Double Layer Transistors. *J. Phys. Soc. Jpn.* **2014**, *83*, 032001.

(23) Ye, J. T.; Inoue, S.; Kobayashi, K.; Kasahara, Y.; Yuan, H. T.; Shimotani, H.; Iwasa, Y. Liquid-Gated Interface Superconductivity on an Atomically flat film. *Nat. Mater.* **2010**, *9*, 125.

(24) Ozaki, T.; Wu, L.; Zhang, C.; Jaroszynski, J.; Si, W.; Zhou, J.; Zhu, Y.; Li, Q. A Route for a Strong Increase of Critical Current in Nanostrained Iron-Based Superconductors. *Nat. Commun.* **2016**, *7*, 13036.

(25) Zhang, C.; Si, W.; Li, Q. Doubling the Critical Current Density in Superconducting $FeSe_{0.5}Te_{0.5}$ Thin Films by Low Temperature Oxygen Annealing. *Appl. Phys. Lett.* **2016**, *109*, 202601.

(26) Sun, Y.; Taen, T.; Tsuchiya, Y.; Shi, Z. X.; Tamegai, T. Effects of Annealing, Acid and Alcoholic Beverages on $Fe_{1+y}Te_{0.6}Se_{0.4}$. *Supercond. Sci. Technol.* **2013**, *26*, 015015.

(27) Li, Q.; Si, W.; Dimitrov, I. K. Films of Iron Chalcogenide Superconductors. *Rep. Prog. Phys.* **2011**, *74*, 124510.

(28) Liu, T. J.; Hu, J.; Qian, B.; Fobes, D.; Mao, Z. Q.; Bao, W.; Reehuis, M.; Kimber, S. A. J.; Prokeš, K.; Matas, S.; Argyriou, D. N.; Hiess, A.; Rotaru, A.; Pham, H.; Spinu, L.; Qiu, Y.; Thampy, V.; Savici, A. T.; Rodriguez, J. A.; Broholm, C. From (π,0) Magnetic Order to Superconductivity with (π,π) Magnetic Resonance in $Fe_{1.02}Te_{1-x}Se_x$. *Nat. Mater.* **2010**, *9*, 718−720.

DOI: 10.1021/acsami.9b02373
ACS Appl. Mater. Interfaces 2019, 11, 17979−17986

(29) Si, W.; Lin, Z.-W.; Jie, Q.; Yin, W.-G.; Zhou, J.; Gu, G.; Johnson, P. D.; Li, Q. Enhanced Superconducting Transition Temperature in $FeSe_{0.5}Te_{0.5}$ Thin Films. *Appl. Phys. Lett.* **2009**, *95*, 052504.
(30) Si, W.; Zhou, J.; Jie, Q.; Dimitrov, I.; Solovyov, V.; Johnson, P. D.; Jaroszynski, J.; Matias, V.; Sheehan, C.; Li, Q. Iron-Chalcogenide $FeSe_{0.5}Te_{0.5}$ Coated Superconducting Tapes for High Field Applications. *Appl. Phys. Lett.* **2011**, *98*, 262509.
(31) Si, W.; Han, S. J.; Shi, X.; Ehrlich, S. N.; Jaroszynski, J.; Goyal, A.; Li, Q. High Current Superconductivity in $FeSe_{0.5}Te_{0.5}$ Coated-Conductors at 30 Tesla. *Nat. Commun.* **2013**, *4*, 1347.
(32) Fedorov, M. V.; Kornyshev, A. A. Towards Understanding the Structure and Capacitance of Electrical Double Layer in Ionic Liquids. *Electrochim. Acta* **2008**, *53*, 6835−6840.
(33) Ivanistsev, V.; Fedorov, M. V. Interfaces Between Charged Surfaces and Ionic Liquids: Insights from Molecular Simulations. *Interface Mag.* **2014**, *23*, 65−69.
(34) Bazant, M. Z.; Storey, B. D.; Kornyshev, A. A. Double Layer in Ionic Liquids: Overscreening versus Crowding. *Phys. Rev. Lett.* **2011**, *106*, 046102.
(35) Bi, S.; Wang, R.; Liu, S.; Yan, J.; Mao, B.; Kornyshev, A. A.; Feng, G. Minimizing the Electrosorption of Water From Humid Ionic Liquids on Electrodes. *Nat. Commun.* **2018**, *9*, 5222.
(36) Péan, C.; Merlet, C.; Rotenberg, B.; Madden, P. A.; Taberna, P.-L.; Daffos, B.; Salanne, M.; Simon, P. On the Dynamics of Charging in Nanoporous Carbon-Based Supercapacitors. *ACS Nano* **2014**, *8*, 1576−1583.
(37) Vatamanu, J.; Borodin, O.; Smith, G. D. Molecular Insights into the Potential and Temperature Dependences of the Differential Capacitance of a Room-Temperature Ionic Liquid at Graphite Electrodes. *J. Am. Chem. Soc.* **2010**, *132*, 14825−14833.
(38) Alam, M. T.; Islam, M. M.; Okajima, T.; Ohsaka, T. Measurements of Differential Capacitance at Mercury/Room-Temperature Ionic Liquids Interfaces. *J. Phys. Chem. C* **2007**, *111*, 18326−18333.
(39) Silva, F.; Gomes, C.; Figueiredo, M.; Costa, R.; Martins, A.; Pereira, C. M. The Electrical Eouble Layer at the $[BMIM][PF_6]$ Ionic Liquid/Electrode Interface − Effect of Temperature on the Differential Capacitance. *J. Electroanal. Chem.* **2008**, *622*, 153−160.
(40) Lockett, V.; Sedev, R.; Ralston, J.; Horne, M.; Rodopoulos, T. Differential Capacitance of the Electrical Double Layer in Imidazolium-Based Ionic Liquids: Influence of Potential, Cation Size, and Temperature. *J. Phys. Chem. C* **2008**, *112*, 7486−7495.
(41) Lin, R.; Taberna, P.-L.; Fantini, S.; Presser, V.; Pérez, C. R.; Malbosc, F.; Rupesinghe, N. L.; Teo, K. B. K.; Gogotsi, Y.; Simon, P. Capacitive Energy Storage from −50 to 100 °C Using an Ionic Liquid Electrolyte. *J. Phys. Chem. Lett.* **2011**, *2*, 2396−2401.
(42) Feng, G.; Li, S.; Atchison, J. S.; Presser, V.; Cummings, P. T. Molecular Insights into Carbon Nanotube Supercapacitors: Capacitance Independent of Voltage and Temperature. *J. Phys. Chem. C* **2013**, *117*, 9178−9186.
(43) Holovko, M.; Kapko, V.; Henderson, D.; Boda, D. On the Influence of Ionic Association on the Capacitance of an Electrical Double Layer. *Chem. Phys. Lett.* **2001**, *341*, 363−368.
(44) Bellingeri, E.; Kawale, S.; Braccini, V.; Buzio, R.; Gerbi, A.; Martinelli, A.; Putti, M.; Pallecchi, I.; Balestrino, G.; Tebano, A.; Ferdeghini, C. Tuning of the Superconducting Properties of $FeSe_{0.5}Te_{0.5}$ Thin Films through the Substrate Effect. *Supercond. Sci. Technol.* **2012**, *25*, 084022.
(45) Ge, J.-F.; Liu, Z.-L.; Liu, C.; Gao, C.-L.; Qian, D.; Xue, Q.-K.; Liu, Y.; Jia, J.-F. Superconductivity above 100 K in single-layer FeSe films on doped SrTiO3. *Nat. Mater.* **2015**, *14*, 285.
(46) Merlet, C.; Péan, C.; Rotenberg, B.; Madden, P. A.; Daffos, B.; Taberna, P. L.; Simon, P.; Salanne, M. Highly Confined Ions Store Charge More Efficiently in Supercapacitors. *Nat. Commun.* **2013**, *4*, 2701.
(47) Merlet, C.; Rotenberg, B.; Madden, P. A.; Taberna, P.-L.; Simon, P.; Gogotsi, Y.; Salanne, M. On the Molecular Origin of Supercapacitance in Nanoporous Carbon Electrodes. *Nat. Mater.* **2012**, *11*, 306.
(48) Lopes, J. N. C.; Pádua, A. A. H. Molecular Force Field for Ionic Liquids Composed of Triflate or Bistriflylimide Anions. *J. Phys. Chem. B* **2004**, *108*, 16893−16898.
(49) Heinz, H.; Vaia, R. A.; Farmer, B. L.; Naik, R. R. Accurate Simulation of Surfaces and Interfaces of Face-Centered Cubic Metals Using 12−6 and 9−6 Lennard-Jones Potentials. *J. Phys. Chem. C* **2008**, *112*, 17281−17290.
(50) Hess, B.; Kutzner, C.; van der Spoel, D.; Lindahl, E. GROMACS 4: Algorithms for Highly Efficient, Load-Balanced, and Scalable Molecular Simulation. *J. Chem. Theory Comput.* **2008**, *4*, 435−447.
(51) Hess, B.; Bekker, H.; Berendsen, H. J. C.; Fraaije, J. G. E. M. LINCS: A Linear Constraint Solver for Molecular Simulations. *J. Comput. Chem.* **1997**, *18*, 1463−1472.
(52) Bussi, G.; Donadio, D.; Parrinello, M. Canonical Sampling Through Velocity Rescaling. *J. Chem. Phys.* **2007**, *126*, 014101.
(53) Raghunathan, A. V.; Aluru, N. R. Self-Consistent Molecular Dynamics Formulation for Electric-Field-Mediated Electrolyte Transport through Nanochannels. *Phys. Rev. E: Stat., Nonlinear, Soft Matter Phys.* **2007**, *76*, 011202.
(54) Tokuda, H.; Hayamizu, K.; Ishii, K.; Susan, M. A. B. H.; Watanabe, M. Physicochemical Properties and Structures of Room Temperature Ionic Liquids. 2. Variation of Alkyl Chain Length in Imidazolium Cation. *J. Phys. Chem. B* **2005**, *109*, 6103−6110.
(55) Fredlake, C. P.; Crosthwaite, J. M.; Hert, D. G.; Aki, S. N. V. K.; Brennecke, J. F. Thermophysical Properties of Imidazolium-Based Ionic Liquids. *J. Chem. Eng. Data* **2004**, *49*, 954−964.
(56) Dzyuba, S. V.; Bartsch, R. A. Influence of Structural Variations in 1-Alkyl(aralkyl)-3-Methylimidazolium Hexafluorophosphates and Bis(trifluoromethylsulfonyl)imides on Physical Properties of the Ionic Liquids. *ChemPhysChem* **2002**, *3*, 161−166.
(57) Zhang, S.; Zhang, J.; Zhang, Y.; Deng, Y. Nanoconfined Ionic Liquids. *Chem. Rev.* **2017**, *117*, 6755−6833.
(58) Singh, M. P.; Singh, R. K.; Chandra, S. Properties of ionic liquid confined in porous silica matrix. *ChemPhysChem* **2010**, *11*, 2036−2043.
(59) Kanakubo, M.; Hiejima, Y.; Minami, K.; Aizawa, T.; Nanjo, H. Melting Point Depression of Ionic Liquids Confined in Nanospaces. *Chem. Commun.* **2006**, 1828−1830.
(60) Si, W.; Zhang, C.; Shi, X.; Ozaki, T.; Jaroszynski, J.; Li, Q. Grain Boundary Junctions of $FeSe_{0.5}Te_{0.5}$ Thin Films on $SrTiO_3$ Bi-Crystal Substrates. *Appl. Phys. Lett.* **2015**, *106*, 032602.

DOI: 10.1021/acsami.9b02373
ACS Appl. Mater. Interfaces 2019, 11, 17979−17986